IRSTI 27.41.19 https://doi.org/10.26577/ijmph.20210126

Fractional-Order Supercapacitor Modeling for High-Power eVTOL Applications Using GCD-Based Chebyshev–Galerkin Spectral Analysis

Ahmed Taleb Mohamed [1], **Omar Mokhtar** [2], **Ahmed M. Taiea** [3,4], **Ayoub Elajjani** [4], **Kairzhan Karzhaubayev** [5,6] **and Alamir H. Hassan** [3,4*]

[1] *Department of Electrical Power Engineering, Faculty of Engineering, Cairo University, Giza, 12613, Egypt*
[2] *Department of Physics and Engineering Mathematics, Faculty of Engineering–Mataria, Capital University (formerly Helwan University), Cairo, 11718, Egypt*
[3] *Mechanical Power Engineering Department, Faculty of Engineering–Mataria, Capital University (formerly Helwan University), Cairo, 11718, Egypt*
[4] *Department of Mechanical and Energy Engineering, Southern University of Science and Technology, Shenzhen 518055, China*
[5] *Department of Mathematical and Computer Modeling, Farabi University, Almaty, 050040, Kazakhstan*
[6] *Department of Software Engineering, International Engineering and Technological University, Almaty, 050060, Kazakhstan*

Email: alamirhoussin@m-eng.capu.edu.eg

(Received 21 September 2026; revised 31 October 2026; accepted 5 November 2026)

Abstract. The rapid development of electric vertical takeoff and landing (eVTOL) vehicles has increased the demand for high-power, lightweight, and fast-response energy storage systems capable of handling severe transient loads. Supercapacitors have emerged as a promising solution in hybrid energy storage systems due to their high-power density, rapid charge–discharge capability, and long cycle life. However, their electrochemical dynamics exhibit strong fractional-order behavior caused by anomalous ion diffusion and the fractal electrode–electrolyte interface, making accurate numerical modeling challenging for conventional methods. This paper presents an improved GCD-based Chebyshev–Galerkin spectral framework for solving the fractional integro-differential equations (FIDEs) governing electric double-layer capacitor (EDLC) dynamics under the constant phase element (CPE) model. The proposed method constructs a generalized fractional Chebyshev basis that spans a truncated fractional-power trial space adapted to the Caputo derivative, thereby improving representation of fractional-power behavior relative to standard polynomial bases. In addition, a graded Gauss–Legendre quadrature strategy is introduced to accurately resolve the singular behavior near the initial charging stage. Three numerical approaches are comparatively investigated: the finite-difference L1 scheme, the standard Chebyshev–Galerkin method, and the proposed GCD-based spectral method. For the representative supercapacitor model with fractional order $\alpha = 0.75$, the proposed approach achieves a maximum error of 4.2×10^{-3} using only 7 degrees of freedom, whereas the standard Chebyshev–Galerkin method has a larger reported error even at higher basis orders, and the finite-difference method requires more than 500 degrees of freedom for comparable performance. The reported results demonstrate improved error per degree of freedom for the tested case. The measured error reaches a plateau at higher basis orders, and real-time suitability remains to be established by processor-specific runtime benchmarking.

Keywords: Supercapacitor modeling; Fractional-order systems; Chebyshev–Galerkin method; Spectral numerical methods.

Introduction

The rapid growth of urbanization and vehicle ownership has made urban traffic mobility increasingly congested, creating significant challenges for conventional ground transportation systems [1, 2]. To address these limitations, urban air mobility (UAM) has emerged as a promising solution by utilizing three-dimensional (3-D) airspace to improve transportation efficiency and reduce travel time [2, 3]. Among the most important enabling technologies for UAM, electric vertical takeoff and landing (eVTOL) aircraft have attracted considerable attention due to their flexible operation, high energy efficiency, reduced environmental impact, and suitability for short-range urban transportation [1, 3]. However, the severe transient power demands during takeoff, landing, hovering, and emergency maneuvers require advanced onboard energy storage systems capable of delivering high power density,

 © 2026 Al-Farabi Kazakh National University

rapid charge–discharge response, and long operational lifetime. Supercapacitors have emerged as a highly attractive solution for such high-power applications because they store energy through the electric double-layer (EDL) mechanism using high-surface-area porous electrodes, enabling significantly higher capacitance than conventional dielectric capacitors while preserving fast dynamic response and high-power density. These characteristics have enabled successful deployment in grid stabilization systems [4], hybrid electric vehicles [5], and power electronics applications requiring rapid transient support. As the role of supercapacitors expands in high-power eVTOL platforms, accurate dynamic modeling becomes essential for system design, performance prediction, real-time control, and energy management optimization. Existing supercapacitor models are generally classified into two main categories: equivalent circuit models and physics-based models.

Equivalent circuit (EC) models represent one of the most widely used approaches for supercapacitor modeling due to their structural simplicity and low computational cost. These models typically employ parameterized resistor–capacitor (RC) networks to reproduce the electrical behavior of the device under specific operating conditions, as presented in [6, 7]. Their main advantage lies in their simplicity, which makes them attractive for fast simulation, control implementation, and preliminary system design. However, representing a complex electrochemical energy storage device using simplified RC circuits introduces several limitations. First, the model states have no direct physical interpretation, making it difficult to extract electrochemical insight or improve the model structure based on physical behavior. Second, EC models are strongly dependent on parameter identification under specific operating conditions, and their accuracy deteriorates significantly when the operating environment changes. This black-box representation limits their effectiveness in advanced control strategies, observer design, and high-fidelity energy management systems for eVTOL applications.

In contrast, physics-based models describe supercapacitor dynamics using conservation laws, ion transport mechanisms, and diffusion equations, typically formulated as coupled partial differential equations (PDEs) with algebraic constraints. This approach provides stronger physical interpretability and improved generalization across varying operating conditions, making model development, control design, and state estimation more reliable. Several studies have investigated such models using different numerical frameworks. Experimental validation of PDE-based solutions was reported in [8], while the computational implementation introduced in [9] established a foundation for subsequent developments. Multi-physics modeling using COMSOL was explored in [10] for non-binary electrolytes, and a volume-averaging finite-element formulation was proposed in [11] to extend the model to higher spatial dimensions. A comparative assessment in [12] demonstrated that spectral methods provide superior accuracy relative to finite-difference and finite-element approaches for a fixed discretization size. Analytical solutions under constrained operating conditions were derived in [13], and commercial modeling platforms were reviewed in [14]. Beyond numerical solution strategies, physics-based and reduced-order models have also been integrated within state estimation and control frameworks. An Extended Kalman Filter (EKF) applied to equivalent circuit representations in [15] improved energy prediction accuracy compared to the conventional expression $E = \frac{1}{2}CV^2$. In related battery systems, observer-based methodologies have been extensively developed for power management applications [16], including nonlinear moving horizon estimation strategies for reduced-order models [17]. These advancements highlight the importance of accurate and computationally efficient models for real-time estimation and control. Despite these developments, the high computational burden associated with PDE-based formulations remains a critical limitation, particularly for real-time onboard applications in power electronics and energy management systems.

In recent years, fractional calculus has emerged as an effective mathematical framework for modeling physical and engineering systems characterized by memory effects and hereditary behavior, where classical integer-order models fail to provide sufficient accuracy [18, 19]. Fractional-order derivatives have been successfully applied in viscoelasticity [18, 19], electromagnetic wave propagation [20], econometric long-memory processes [21], nanoparticle interfaces [22], dielectric polarization [23], as well as in bioengineering, robotics, and seismic analysis. Among these applications, electric double-layer capacitors (EDLCs), commonly referred to as supercapacitors, represent one of the most important emerging areas of fractional-order modeling. Unlike conventional capacitors, supercapacitors exhibit strong fractional dynamic behavior due to anomalous ion diffusion through porous electrode structures and the fractal geometry of the electrode–electrolyte interface. This behavior is accurately represented by the Constant Phase Element (CPE) model, where the voltage dynamics are governed by fractional integro-differential equations (FIDEs) involving a Caputo derivative of non-integer order $\alpha \in (0, 1)$.

Related work published in the International Journal of Mathematics and Physics provides mathematical context for fractional-order physical models. Ruzhansky, Serikbaev, and Tokmagambetov examined an inverse problem for a time-fractional pseudo-parabolic equation involving the Caputo derivative [24]. Elma and Misirli obtained traveling-wave solutions of a conformable fractional modified Camassa–Holm equation using analytical techniques [25]. The latter work employs a conformable derivative rather than the Caputo operator used here; neither study addresses fractional Chebyshev trial spaces for supercapacitor voltage dynamics.

Numerical techniques for related fractional differential equations also include Khader's treatment of the fractional Riccati equation [26], the fractional-order Legendre functions of Kazem et al. [27], and Chebyshev spectral methods for multi-term fractional differential equations developed by Doha et al. [28]. Related operational-matrix formulations were investigated by Bhrawy and Alofi using shifted Chebyshev polynomials [29] and by Akrami et al. using shifted Legendre polynomials [30]. These works provide numerical-method context, without directly addressing the present supercapacitor model.

Accurate numerical solutions of these FIDEs are essential for real-time supercapacitor management systems, power electronics design, and hybrid energy storage optimization in high-power eVTOL applications. Several numerical approaches have been proposed for solving such equations. In related numerical analysis within this journal, Tankeyeva and Mynbayeva developed a parameterization-based computational method for an impulsive Fredholm integro-differential boundary-value problem, reducing its formulation to auxiliary differential problems and an algebraic system [31]. Although the governing equation and boundary conditions differ from the Caputo–Volterra model considered here, this study provides relevant context for computational treatments of integro-differential equations.

Momani and Qaralleh [32] applied the Adomian decomposition method to fractional integrodifferential systems. Javeed et al. [33] analyzed the homotopy perturbation method for fractionalorder differential equations, while Diethelm and Ford [34] investigated the analysis of fractional differential equations. Nazari and Shahmorad [35] developed a fractional differential transform approach for fractional-order integro-differential equations with nonlocal boundary conditions. In the context of spectral methods, Youssri and Atta [36] formulated a Chebyshev Petrov–Galerkin method for nonlinear time-fractional integrodifferential equations with a mildly singular kernel. However, the supercapacitor FIDE solution involves the Mittag–Leffler function and exhibits a fractional-power singularity of the form t^{α} near the origin. Since the standard polynomial Chebyshev basis spans only integer powers of t, a basis–solution mismatch occurs, causing the standard method to lose spectral

convergence and exhibit only slow algebraic convergence. This limitation significantly reduces computational efficiency and restricts practical real-time implementation in engineering applications. To overcome these limitations, this paper presents an improved GCD-based Chebyshev–Galerkin spectral framework for fractional-order supercapacitor modeling in high-power eVTOL applications. The main contributions of this work are summarized as follows:

1. The proposed method specifically addresses the basis–solution mismatch that limits the performance of conventional polynomial spectral methods for non-integer singular solutions.

2. For rational fractional orders $\alpha = p/q$, a generalized Chebyshev denominator (GCD) basis is constructed using the transformation $\phi_j(t) = T_j\left(2\left(\frac{t}{T}\right)^{\beta} - 1\right), \beta = \frac{1}{q}$ which spans a truncated rational-power trial space. The resulting basis represents the fractional components of the Mittag–Leffler response efficiently in the reported low-order tests, without establishing a uniform asymptotic convergence rate.

3. A graded Gauss–Legendre quadrature strategy is introduced to accurately evaluate the singular fractional derivative behavior near the initial charging stage, where conventional Gaussian quadrature loses accuracy. This enables exact analytical treatment of the Caputo derivative and closed-form evaluation of the Volterra integral term, supporting quadrature of the transformed weakly singular terms.

4. The proposed method is systematically compared with the finite-difference L1 scheme and the standard Chebyshev–Galerkin method using the electric double-layer capacitor (EDLC) model. The reported results demonstrate an error-per-degree-of-freedom advantage for the tested configurations. No processor-runtime or matrix-conditioning measurements are supplied, so real-time suitability remains unverified.

Unified Taxonomy Framework

Fig. 1 illustrates the fundamental distinction between conventional electrostatic capacitors and supercapacitors. In classical capacitors, energy is stored through charge separation across a dielectric medium, resulting in purely electrostatic behavior, as shown in Fig. 1(a). In contrast, supercapacitors rely on the electrochemical double-layer (EDL) mechanism, where charge accumulation occurs at the electrode–electrolyte interface within highly porous structures, as depicted in Fig. 1(b). This distributed structure induces complex ion-transport dynamics, giving rise to non-ideal and fractional-order electrical behavior.

The underlying electrochemical dynamics of supercapacitors are governed by coupled ion transport and charge conservation phenomena within porous electrodes and electrolyte regions. These processes are commonly described using the Nernst–Planck framework combined with electroneutrality and conservation laws [8, 37]. Rather than presenting the full electrochemical derivation, the model can be expressed in a reduced macroscopic form by introducing the electrolyte concentration $c(x,t)$ and the potential difference $\psi(x,t) = \phi_1 - \phi_2$, where ϕ_1 and ϕ_2 denote the solid and liquid phase potentials, respectively.

The resulting system can be compactly represented as a coupled diffusion–migration model:

$$\varepsilon \frac{\partial c}{\partial t} = D_{\text{eff}} \frac{\partial^2 c}{\partial x^2} - \gamma \frac{\partial \psi}{\partial t} \tag{1}$$

$$\eta \frac{\partial \psi}{\partial t} = \frac{\partial^2 \phi_1}{\partial x^2} \tag{2}$$

$$0 = \frac{\partial \phi_1}{\partial x} + \chi \frac{\partial \phi_2}{\partial x} + \delta \frac{\partial \ln c}{\partial x} + \iota \tag{3}$$

where ε is the porosity, D_{eff} is the effective diffusion coefficient, and η represents the double-layer storage effect. The parameters γ, χ, and δ reflect electrochemical coupling, ionic mobility, and thermodynamic effects, respectively, while ι denotes the applied current density.

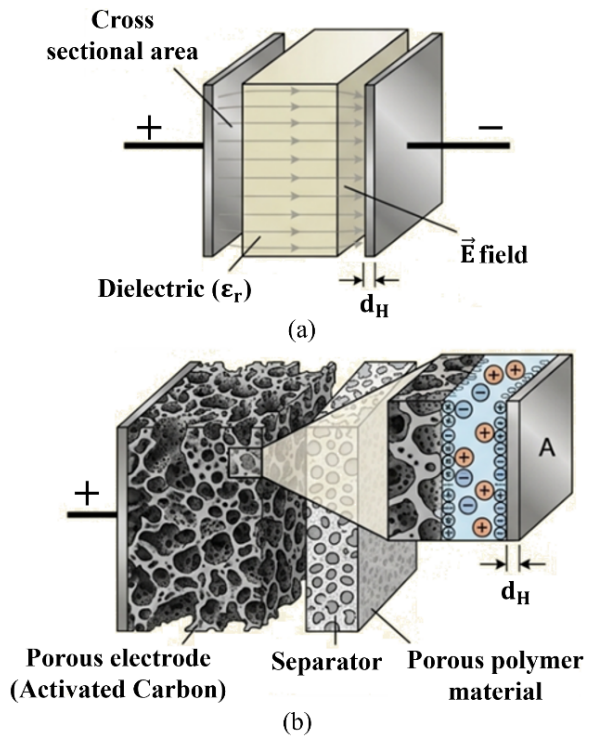


Figure 1 - Comparative energy storage mechanisms: (a) conventional electrostatic capacitor and (b) supercapacitor based on the electrochemical double-layer effect.

Equations (1)–(3) define a nonlinear coupled partial differential equation (PDE) system describing ion diffusion, potential distribution, and charge transfer within the supercapacitor. In the separator region, the model reduces to a diffusion-dominated equation due to the absence of electronic conduction.

The electrochemical parameters used in this study are summarized in Table 1, while the region-specific properties are given in Table 2.

Although the distributed model provides high physical fidelity, its computational complexity makes it unsuitable for real-time applications such as onboard energy management in eVTOL systems. To enable efficient simulation while preserving the dominant electrochemical behavior, the model is reduced to a fractional-order representation based on the Constant Phase Element (CPE) concept [14].

Accordingly, the terminal voltage dynamics are described by the following fractional integro-differential equation:

Table 1 – Main Parameters of the Supercapacitor Model [8].

Parameter	Value	Unit
Electrode thickness	50	μm
Separator thickness	25	μm
Specific capacitance	42×10^6	F/m^3
Initial concentration	930	mol/m^3
Conductivity	0.067	S/m
Current density	36.403	A/m^2
Temperature	298	K
Characteristic time	7.4	s

Table 2 – Electrode and Separator Parameters [8].

Region	Parameter	Value
Electrode	Porosity	0.67
Electrode	Conductivity	0.0521 S/m
Separator	Porosity	0.6
Separator	Tortuosity factor	1.29

$$C D_t^{\alpha} v(t) + \lambda v(t) + \mu \int_0^t v(\tau)\, d\tau = \lambda V_s, \quad 0 < t \le T_f, \tag{4}$$

with the initial condition:

$$v(0) = 0 \tag{5}$$

where D_t^{α} denotes the Caputo fractional derivative of order $0 < \alpha < 1$, $v(t)$ is the supercapacitor voltage, and λ and μ are equivalent parameters capturing resistive and capacitive effects. This formulation preserves the intrinsic memory behavior arising from ion diffusion in porous electrodes while enabling efficient numerical treatment.

The fractional model in (4) constitutes the mathematical foundation for the proposed GCD-based Chebyshev–Galerkin method developed in the following section.

Numerical Methodology

The fractional supercapacitor model in (4) is solved using three schemes: the finite-difference L1 method [38], the standard Chebyshev–Galerkin method [36], and the proposed GCD-based Chebyshev–Galerkin method. The first two

methods are used as benchmarks, whereas the third method represents the main contribution of this work.

For a different, nonfractional evolution problem with an integral boundary condition, Koroche analyzed a Lax–Wendroff finite-difference scheme with Richardson extrapolation [39]. That scheme is not the Caputo L1 method employed below, but it illustrates related numerical treatment of integral constraints and convergence errors.

Finite-Difference L1 Reference Scheme

Let T_f be divided into M uniform intervals with

$$h = \frac{T_f}{M}, t_n = nh, v_n \approx v(t_n), n = 0,1,\ldots,M \quad (6)$$

For $0 < \alpha < 1$, the Caputo derivative is approximated by the L1 convolution formula:

$$D_t^{\alpha} v(t_n) \approx \frac{1}{h^{\alpha}\Gamma(2-\alpha)} \sum_{k=0}^{n} a_k^{(\alpha)} v_{n-k} \quad (7)$$

where

$$a_0^{(\alpha)} = 1 \quad (8)$$

$$a_k^{(\alpha)} = (k+1)^{1-\alpha} - 2k^{1-\alpha} + (k-1)^{1-\alpha}, \quad 1 \le k \le n-1 \quad (9)$$

$$a_n^{(\alpha)} = (n-1)^{1-\alpha} - n^{1-\alpha} \quad (10)$$

The Volterra term is approximated as:

$$\int_0^{t_n} v(\xi)\, d\xi \approx h \sum_{r=0}^{n} \rho_r^{(n)} v_r \quad (11)$$

with

$$\rho_0^{(n)} = \rho_n^{(n)} = \frac{1}{2}, \rho_r^{(n)} = 1, 1 \le r \le n-1 \quad (12)$$

Substituting (7) and (11) into (4) gives:

$$v_n = \frac{\lambda V_s - \frac{1}{h^{\alpha}\Gamma(2-\alpha)} \sum_{k=1}^{n} a_k^{(\alpha)} v_{n-k} - \mu h \sum_{r=0}^{n-1} \rho_r^{(n)} v_r}{\frac{1}{h^{\alpha}\Gamma(2-\alpha)} + \lambda + \frac{\mu h}{2}} \quad (13)$$

This scheme provides the reference solution because it directly preserves the nonlocal memory kernel; however, its algebraic convergence requires large M for high accuracy.

Standard Chebyshev–Galerkin Scheme

The shifted Chebyshev basis over $[0, T_f]$ is defined as:

$$T_j(t) = T_j\left(\frac{2t}{T_f} - 1\right), j = 0,1,\ldots,N \quad (14)$$

where $T_j(\cdot)$ denotes the Chebyshev polynomial of the first kind. The approximation is written as:

$$v_N(t) = \sum_{j=0}^{N} \theta_j T_j(t) \quad (15)$$

Using the weighted inner product:

$$\langle f, g \rangle_{\omega} = \int_0^{T_f} \frac{f(t)g(t)}{\sqrt{T_f t - t^2}}\, dt \quad (16)$$

the Galerkin projection becomes:

$$\sum_{j=0}^{N} \theta_j [\langle D_t^{\alpha} T_j, T_m \rangle_{\omega} + \lambda \langle T_j, T_m \rangle_{\omega} + \mu \langle V T_j, T_m \rangle_{\omega}] = \lambda V_s \langle 1, T_m \rangle_{\omega} \quad (17)$$

where

$$VT_j(t) = \int_0^t T_j(\xi)\, d\xi \tag{18}$$

The inner products are evaluated using Gauss–Chebyshev quadrature:

$$\langle f, g\rangle_\omega \approx \frac{\pi}{N_q} \sum_{\ell=1}^{N_q} f(\zeta_\ell) g(\zeta_\ell) \tag{19}$$

where

$$\zeta_\ell = \frac{T_f}{2}\left[1 + \cos\left(\frac{(2\ell-1)\pi}{2N_q}\right)\right] \tag{20}$$

The initial condition is imposed as:

$$\sum_{j=0}^{N} \theta_j T_j(0) = \sum_{j=0}^{N} (-1)^j \theta_j = 0 \tag{21}$$

To enforce the initial condition without adding a row to a full square Galerkin system, we replace the final residual equation by the initial-condition equation. The resulting square system is

$$\widetilde{\mathbf{S}}\theta = \widetilde{\mathbf{r}} \tag{22}$$

For $0 \le m < N$, set $\widetilde{\mathbf{S}}_{m,:} = \mathbf{S}_{m,:}$ and $\widetilde{r}_m = r_m$; for $m = N$, use $\widetilde{\mathbf{S}}_{N,:} = \mathbf{d}^T$ and $\widetilde{r}_N = 0$. The unmodified Galerkin matrix and load entries are

$$S_{mj} = \langle D_t^\alpha T_j, T_m\rangle_\omega + \lambda\langle T_j, T_m\rangle_\omega + \mu\langle VT_j, T_m\rangle_\omega \tag{23}$$

$$r_m = \lambda V_s \langle 1, T_m\rangle_\omega, \qquad d_j = (-1)^j \tag{24}$$

Because the exact supercapacitor response contains fractional powers generated by the Mittag–Leffler structure, the integer polynomial basis in (14) cannot efficiently represent the near-origin behavior. Therefore, the standard Chebyshev–Galerkin method loses spectral convergence and becomes algebraically limited.

Proposed GCD-Based Chebyshev–Galerkin Scheme

To remove the basis–solution mismatch, the proposed method introduces a fractional Chebyshev basis matched to the fractional order. For

$$\alpha = \frac{p}{q}, \quad 0 < p < q, \quad \gcd(p,q) = 1, \quad \beta = \frac{1}{q}, \tag{25}$$

the GCD basis is defined as

$$\Phi_j(t) = T_j\left[2\left(\frac{t}{T_f}\right)^\beta - 1\right], j = 0, 1, \ldots, N. \tag{26}$$

Since $T_j(2x-1)$ is a polynomial of degree j in x, (26) admits the expansion

$$\Phi_j(t) = \sum_{k=0}^{j} \omega_{jk} \left(\frac{t}{T_f}\right)^{k\beta}, \tag{27}$$

where ω_{jk} are the transformed Chebyshev coefficients. Hence,

$$\operatorname{span}\{\Phi_0, \Phi_1, \ldots, \Phi_N\} = \operatorname{span}\{1, t^\beta, t^{2\beta}, \ldots, t^{N\beta}\}. \tag{28}$$

For $\alpha = 3/4$, $\beta = 1/4$, and the basis directly contains the fractional lattice $\left\{t^{k/4}\right\}$ required to represent the dominant solution components.

The proposed approximation is

$$v_N(t) = \sum_{j=0}^{N} \vartheta_j \Phi_j(t). \tag{29}$$

The Caputo derivative of the fractional monomial is evaluated analytically as

$$D_t^\alpha t^{k\beta} = \frac{\Gamma(k\beta+1)}{\Gamma(k\beta-\alpha+1)} t^{k\beta-\alpha}, \quad k \ge 1 \tag{30}$$

For the constant term, the Caputo derivative is zero. The formula for positive powers is integrable for the present orders, although its value can be singular as time approaches zero.

Therefore,

$$D_t^\alpha \Phi_j(t) = \sum_{k=1}^{j} \omega_{jk} \frac{\Gamma(k\beta+1)}{\Gamma(k\beta-\alpha+1)} t^{k\beta-\alpha}. \tag{31}$$

Because $\alpha/\beta = p$ is an integer, the exponent satisfies

$$k\beta - \alpha = (k-p)\beta, \tag{32}$$

The exponent remains on the rational lattice; however, for indices below the numerator, it is negative. Thus, differentiation does not leave the finite-dimensional trial space invariant. The matched basis improves the representation of fractional powers, but this property by itself does not establish a uniform spectral convergence rate.

The Volterra term is also obtained analytically:

$$\begin{aligned} V\Phi_j(t) &= \int_0^t \Phi_j(\xi)\, d\xi \\ &= \sum_{k=0}^{j} \omega_{jk} \frac{T_f}{k\beta+1} \left(\frac{t}{T_f}\right)^{k\beta+1}. \end{aligned} \tag{33}$$

To resolve the singularity near $t = 0$, the integration variable is transformed as

$$t = T_f u^{1/\beta}, 0 \le u \le 1, \tag{34}$$

which gives

$$dt = \frac{T_f}{\beta} u^{1/\beta - 1} du. \tag{35}$$

Thus,

$$\int_0^{T_f} F(t)\, dt = \frac{T_f}{\beta} \int_0^1 F\left(T_f u^{1/\beta}\right) u^{1/\beta - 1}\, du \tag{36}$$

Using Gauss–Legendre nodes $\xi_{\updownarrow}$ and weights $\omega_{\updownarrow}^{GL}$ on $[-1,1]$, define

$$u_\ell = \frac{1+\xi_\ell}{2}, \qquad t_\ell = T_f u_\ell^{1/\beta} \tag{37}$$

and the effective quadrature weights

$$\Omega_\ell = \frac{T_f}{2\beta} \omega_\ell^{GL} u_\ell^{1/\beta - 1} \tag{38}$$

The unweighted Galerkin projection becomes

$$\sum_{j=0}^{N} \vartheta_j \left[\langle D_t^\alpha \Phi_j, \Phi_m \rangle + \lambda \langle \Phi_j, \Phi_m \rangle + \mu \langle V\Phi_j, \Phi_m \rangle \right] = \lambda V_s \langle 1, \Phi_m \rangle, \tag{39}$$

where

$$\langle f, g \rangle = \int_0^{T_f} f(t) g(t)\, dt \tag{40}$$

After graded quadrature, the matrix entries are

$$K_{mj} = \sum_{\ell=1}^{N_q} \Omega_\ell \left[D_t^\alpha \Phi_j(t_\ell) + \lambda \Phi_j(t_\ell) + \mu V\Phi_j(t_\ell) \right] \Phi_m(t_\ell) \tag{41}$$

$$f_m = \lambda V_s \sum_{\ell=1}^{N_q} \Omega_\ell \Phi_m(t_\ell) \tag{42}$$

The initial condition is imposed as

$$\sum_{j=0}^{N} \vartheta_j \Phi_j(0) = \sum_{j=0}^{N} (-1)^j \vartheta_j = 0 \tag{43}$$

The Galerkin matrix has $(N+1)$ rows and $(N+1)$ unknown coefficients. Appending the ini-

tial condition as an extra row would produce a rectangular system, so an ordinary matrix inverse would be invalid. Instead, we enforce the initial condition by replacing the last Galerkin residual row, retaining the equations for $m = 0, \ldots, N-1$:

$$\widetilde{\mathbf{K}}\vartheta = \widetilde{\mathbf{f}}. \tag{44}$$

Specifically, $\widetilde{\mathbf{K}}_{m,:} = \mathbf{K}_{m,:}$ and $\widetilde{f}_m = f_m$ for $0 \le m < N$; the last row is $\widetilde{\mathbf{K}}_{N,:} = \mathbf{b}^T$ and $\widetilde{f}_N = 0$, with $b_j = (-1)^j$. Thus, $\widetilde{\mathbf{K}} \in \mathbb{R}^{(N+1)\times(N+1)}$. Provided the square matrix is nonsingular, the coefficients are obtained by an LU-based linear solve:

$$\vartheta = \mathrm{solve}(\widetilde{\mathbf{K}}, \widetilde{\mathbf{f}}). \tag{45}$$

Algorithm 1. Proposed GCD-Based Chebyshev–Galerkin Spectral Solver

Require: Fractional order $\alpha = p/q$; terminal time T_f; model coefficients λ, μ; source voltage V_s; basis order N; quadrature order N_q.
Ensure: Approximate voltage response $v_N(t)$.

1. Set $\beta = 1/q$ and construct the GCD basis $\{\Phi_j(t)\}_{j=0}^{N}$ using (26).
2. Expand each $\Phi_j(t)$ into the fractional-power lattice using (27).
3. Generate the graded Gauss–Legendre nodes t_ℓ and effective weights Ω_ℓ using (37) and (38).
4. **for** $j = 0$ to N **do**
   (a) Evaluate $D_t^\alpha \Phi_j(t_\ell)$ from (31), $\ell = 1, \ldots, N_q$.
   (b) Evaluate $V\Phi_j(t_\ell)$ from (33), $\ell = 1, \ldots, N_q$.
5. **end for**
6. **for** $m = 0$ to N **do**
   (a) **for** $j = 0$ to N **do**
   (b) Assemble K_{mj} using (41).
   (c) **end for**
   (d) Assemble f_m using (42).
7. **end for**
8. Impose the initial condition through $\mathbf{b}^T\vartheta = 0$, where $b_j = (-1)^j$.
9. Replace the last residual row with the initial-condition row, then solve the square system (44) using LU factorization.
10. Reconstruct $v_N(t) = \sum_{j=0}^{N} \vartheta_j \Phi_j(t)$.
11. **Output:** Return $v_N(t)$.

The implementation steps of the proposed GCD-based Chebyshev–Galerkin solver are summarized in Algorithm 1. The algorithm follows directly from the fractional basis construction, graded quadrature mapping, analytical Caputo derivative evaluation, and square row-replacement assembly developed in (26)–(44).

The proposed GCD-based Chebyshev–Galerkin method overcomes the fundamental limitation of both the L1 finite-difference scheme and the standard CGM by eliminating the basis–solution mismatch inherent in fractional-order models. In the L1 scheme, the Caputo operator is discretized through a history-dependent convolution sum, leading to algebraic convergence $\mathcal{O}(h^{2-\alpha})$ and increasing computational cost due to long-memory accumulation. Similarly, the standard CGM employs integer-order polynomial bases $\left\{T_j^*(t)\right\}$, which are unable to represent the intrinsic fractional behavior $v(t) \sim t^\alpha$ near $t = 0$, resulting in only algebraic decay of the approximation error. In contrast, the proposed GCD basis $\left\{\Phi_j(t)\right\}$ spans fractional power space $\left\{t^{k\beta}\right\}$ with $\beta = 1/q$, ensuring that both the solution and its Caputo derivative remain within the same functional space, i.e., $D_t^\alpha t^{k\beta} \propto t^{(k-p)\beta}$, which maps powers onto the same exponent lattice, although negative powers can arise. This property enables termwise analytical evaluation of the fractional operator and supports rapid error reduction at low orders in the present tests, but does not prove asymptotic spectral convergence. Furthermore, the graded transformation $t = T_f u^{1/\beta}$ concentrates quadrature nodes near the singularity, yielding accurate integration of weakly singular kernels. Consequently, the proposed method achieves lower reported error at matched degrees of freedom in the tested case;

Table 3 – Validation parameters for the representative supercapacitor case.

Parameter	Value	Unit	Description
C_α	100	$F/s^{1-\alpha}$	Fractional pseudo-capacitance
R	0.05	Ω	Equivalent series resistance
α	0.75	–	Fractional order
V_s	5	V	Source voltage
$v(0)$	0	V	Initial voltage

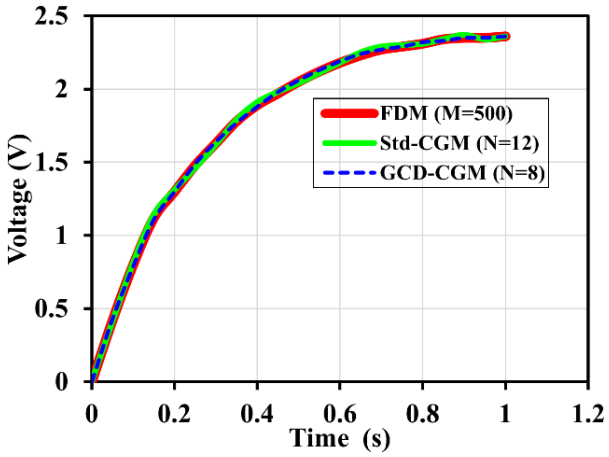


Figure 2 - Voltage response comparison obtained using the finite-difference L1 scheme, standard Chebyshev–Galerkin method, and proposed GCD-based Chebyshev–Galerkin method.

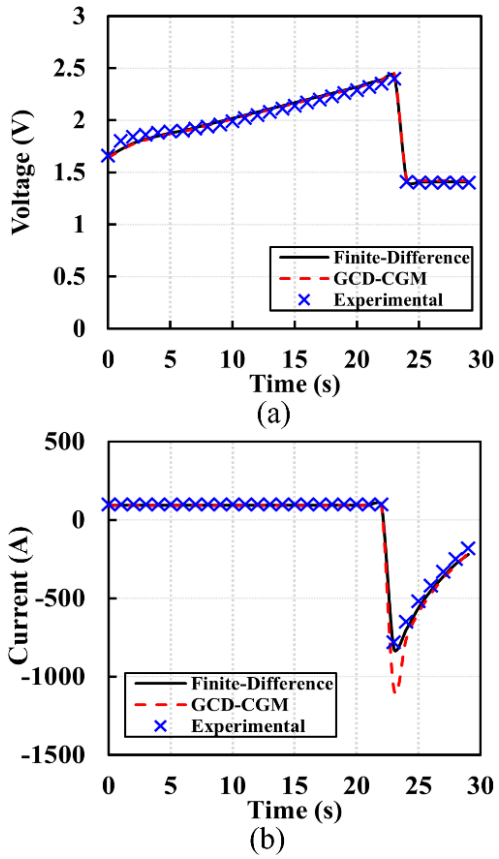


Figure 3 - Experimental validation of voltage and current responses using finite-difference and GCD-CGM solutions against experimental data reported in [8].

a direct conditioning and runtime comparison remains necessary.

Results and Discussion

Validation of the Proposed Method

The proposed GCD-based Chebyshev–Galerkin method is first validated against the finite-difference L1 scheme and the standard Chebyshev–Galerkin method. The main simulation parameters used for the representative supercapacitor case are summarized in Table 3. The fractional order is selected as $\alpha = 0.75$, corresponding to $\beta = 0.25$ in the proposed GCD basis.

The voltage responses in Fig. 2 show that the proposed GCD-CGM closely follows the reference solution obtained using a substantially large number of degrees of freedom. For the same test case, FDM with $M = 500$, standard CGM with $N = 12$, and GCD-CGM with $N = 8$ yield maximum errors of 8.87×10^{-3}, 4.30×10^{-2}, and 4.61×10^{-3}, respectively. Hence, the proposed method achieves higher accuracy than the standard CGM and comparable accuracy to FDM while using only 9 DOFs instead of 501 DOFs.

The quantitative comparison in Table 4 further confirms the efficiency of the proposed method. With only 7 DOFs, GCD-CGM attains an error of 4.242×10^{-3}, whereas the standard CGM still produces an error of 2.037×10^{-2} even with 21 DOFs. This indicates that the proposed fractional basis is better aligned with the intrinsic Mittag–Leffler-type solution structure.

The experimental comparison in Fig. 3 verifies the physical consistency of the proposed solver. Both FDM and GCD-CGM reproduce the voltage and current profiles reported in [8], including the charging stage and the abrupt current transition. However, the proposed GCD-CGM achieves this agreement using a compact spectral represen-

Table 4 – Final voltage and minimum error comparison among the three numerical methods.

Method	Best N or M	DOFs	Min. error	$v(T)$ (V)
FDM L1	2000	2001	2.511×10^{-3}	2.3599
Standard CGM	20	21	2.037×10^{-2}	2.3796
GCD-CGM	6	7	4.242×10^{-3}	2.3594

tation, whereas conventional spatial discretization methods may require significantly larger element numbers for similar accuracy, as reported in earlier finite-element-based studies [11].

Convergence and Pointwise Error Analysis

The convergence behavior is evaluated using the maximum error

$$\varepsilon_{\max} = \max_{t\in[0,T_f]} |v_N(t) - v_{\mathrm{ref}}(t)| \qquad (46)$$

where $v_{\mathrm{ref}}(t)$ denotes the high-resolution reference solution.

The convergence trends in Fig. 4(a) demonstrate that the L1 scheme follows an algebraic decay consistent with its fractional-memory discretization. The standard CGM also converges algebraically because the polynomial basis $\{T_n(t)\}$ cannot efficiently represent the near-origin fractional singularity t^{α}. In contrast, the GCD-CGM error decreases from approximately 1.1×10^{-1} at low order to 4.2×10^{-3} with only a few basis functions. These data show rapid initial error reduction, not indefinite spectral convergence; the measured errors subsequently level off. The matched-DOF comparison in Fig. 4(b) confirms that GCD-CGM consistently yields the smallest error among the three methods.

The pointwise errors in Fig. 5 reveal the source of the improvement of the convergence. The standard CGM exhibits oscillatory errors in the range of 10^{-2}–10^{-1}, indicating that increasing the polynomial order does not fully remove the fractional singularity mismatch. Conversely, the proposed GCD-CGM produces uniformly lower errors and reaches the FDM $M = 500$ reference level at $N = 7$, while $N = 12$ approaches the FDM $M = 2000$ level. This confirms that the fractional basis directly captures the dominant solution space instead of approximating it through higher-order integer polynomials.

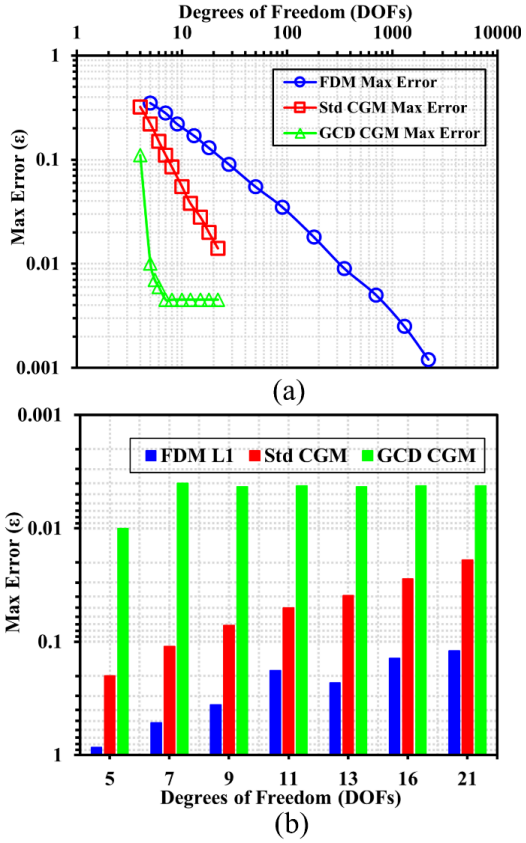


Figure 4 - Convergence comparison of FDM L1, standard CGM, and GCD-CGM: (a) maximum error versus DOFs and (b) maximum error at matched DOF levels.

The parametric results in Table 5 show close agreement between the reported FDM and GCD-CGM terminal voltages across the tabulated fractional orders. The basis exponent listed for the $\alpha = 0.65$ case is not the exact denominator-based value prescribed by Eq. (25): $0.65 = 13/20$ requires $\beta = 1/20 = 0.05$, whereas the supplied results list 0.25. The existing numerical data are retained transparently as a non-matched-basis calculation; a re-run with the prescribed exponent is required before claiming that this row validates the exact GCD construction. The $\alpha = 1$ row is

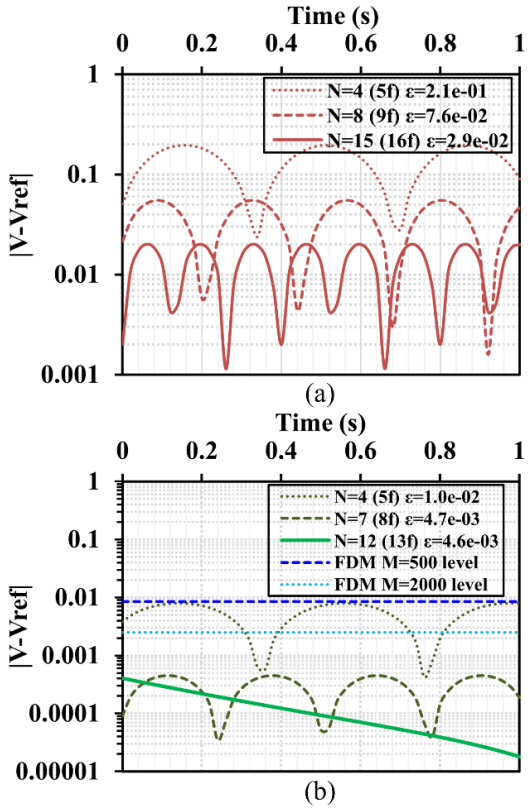


Figure 5 - Pointwise voltage-error comparison: (a) standard CGM at different polynomial orders and (b) proposed GCD-CGM with FDM reference-error levels.

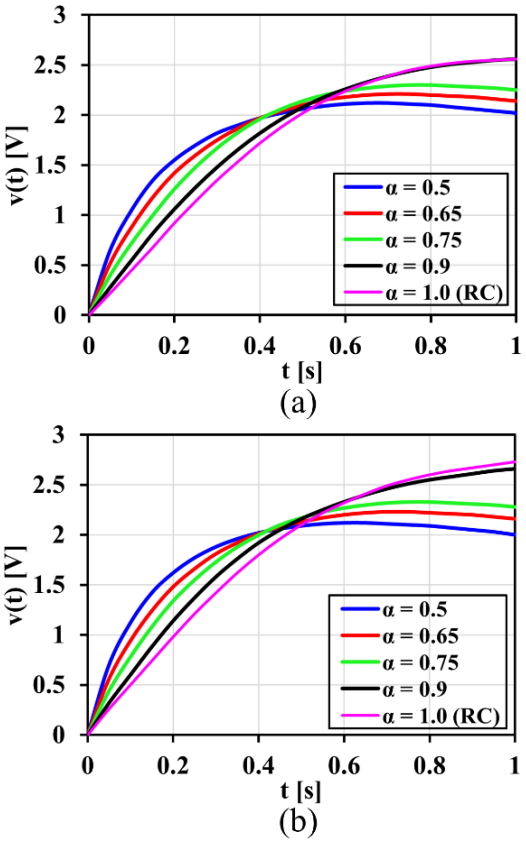


Figure 6 - Effect of fractional order on supercapacitor voltage response: (a) FDM L1 solution and (b) proposed GCD-CGM solution.

an integer-order limiting benchmark rather than a case covered by the stated $0 < \alpha < 1$ derivation. As α approaches unity, the response gradually approaches the classical RC charging behavior. For $\alpha = 0.75$, the terminal voltage reaches approximately 47.2% of the source voltage at $T = 1$ s, whereas the integer-order case reaches approximately 53.35%. This difference quantifies the sub-diffusive memory effect associated with anomalous ion transport in porous electrodes.

Degree-of-Freedom Efficiency

The degree-of-freedom efficiency of the proposed method is evaluated by comparing the standard CGM and GCD-CGM at equal basis orders. The following quantity is the dimensionless error-reduction factor, not a CPU-time speedup:

$$R_{\text{err}} = \frac{\varepsilon_{\text{Std-CGM}}}{\varepsilon_{\text{GCD-CGM}}}. \tag{47}$$

The results in Table 6 show that the GCD-CGM error reaches its smallest reported value at $N = 6$ and subsequently levels off near 4.6×10^{-3} as N increases. Thus, the presented data support a rapid pre-asymptotic decrease but do not show sustained spectral convergence. Plausible error-floor sources include quadrature resolution, the discretization of the reference solution, and finite-precision or linear-solver effects; the supplied results cannot isolate these contributions. A systematic quadrature- and reference-refinement test is needed before assigning a dominant cause or claiming an asymptotic rate. In contrast, the standard CGM improves slowly and remains above 2.0×10^{-2} even at $N = 20$. The largest reported error-reduction factor is 31.2×. This describes a ratio of numerical errors at matched degrees of freedom and must not be interpreted as an execution-time reduction.

The matched-unknown comparison in Table

Table 5 – Final voltage and charging fraction for different fractional orders. The unmatched and limiting cases are identified below.

α	β	**FDM** $v(T)$ **(V)**	**GCD-CGM** $v(T)$ **(V)**	V_s **(V)**	**Charging (%) FDM**	**Charging (%) GCD-CGM**
0.50	0.50	2.042694	2.042578	5	40.8539	40.8516
0.65	0.25†	2.230103	2.229074	5	44.6021	44.5815
0.75	0.25	2.359918	2.359943	5	47.1984	47.1989
0.90	0.10	2.551320	2.551414	5	51.0264	51.0283
1.00‡	0.50	2.667536	2.667536	5	53.3507	53.3507

Dagger: reported unmatched choice; the exact choice for $\alpha = 13/20$ is $\beta = 0.05$ and would require recomputation.

Double dagger: classical $\alpha = 1$ limit, outside the fractional-order derivation.

Table 6 – Equal-order comparison between standard CGM and GCD-CGM for $\alpha = 0.75$ and $\beta = 0.25$.

N	**DOFs**	**Std-CGM** $v(T)$ **(V)**	**GCD-CGM** $v(T)$ **(V)**	**Std-CGM** $\varepsilon_{\max}$	**GCD-CGM** $\varepsilon_{\max}$	R_{err}
3	4	2.281298	2.419605	0.322015	0.113327	2.8×
4	5	2.391355	2.362486	0.212861	0.010333	20.6×
5	6	2.339690	2.358265	0.153113	0.004913	31.2×
6	7	2.371277	2.359378	0.116559	0.004242	27.5×
7	8	2.351282	2.359829	0.092429	0.004662	19.8×
8	9	2.365544	2.359929	0.075557	0.004606	16.4×
10	11	2.363200	2.359943	0.053951	0.004598	11.7×
12	13	2.362041	2.359941	0.041017	0.004599	8.9×
15	16	2.358572	2.359941	0.029297	0.004599	6.4×
20	21	2.379610	2.359941	0.020370	0.004599	4.4×

7 illustrates the error-per-DOF advantage of the proposed method. At 6 DOFs, GCD-CGM improves the error relative to FDM by approximately 68.2×. Even at 16 DOFs, the gain remains above 30×, indicating that the method merits further benchmarking for compact onboard supercapacitor solvers.

Runtime Evidence and Reproducibility Limitations

The numerical comparisons in Tables 4, 6, and 7 report solution error and the number of discretization unknowns, not measured processor time. Therefore, no CPU-speedup factor can be computed from those tables, and a real-time deployment claim would be premature. A reproducible timing comparison would require the same hardware, programming language, precision, solver tolerances, and error target; separate wall-clock measurements for assembly, solution, and (for L1) history evaluation; a repeated-run median and spread; and verification against a common reference solution. Since those runtime measurements were not supplied with the calculations, numerical timing values have not been invented. Real-time deployment is a potential application that remains to be evaluated.

Influence of Fractional Order

The influence of α on the charging response is presented in Fig. 6. Lower values of α produce stronger memory effects and slower voltage rise, while higher values approach the classical RC response. The GCD-CGM solutions remain smooth and physically consistent for all tested fractional orders. In contrast, the FDM response may show minor numerical irregularities when α approaches unity because the L1 convolution weights become increasingly sensitive near the integer-order limit. This behavior demonstrates the advantage of the global spectral representation in preserving response smoothness.

State-Variable Error Assessment

The state-variable accuracy is assessed using the normalized error

$$E_y = \frac{\|y_{\text{num}} - y_{\text{ref}}\|_2}{\|y_{\text{ref}}\|_2}, \qquad y \in \{c, \phi_1, \phi_2\} \quad (48)$$

Table 7 – DOF-efficiency comparison at matched unknown counts.

DOFs	FDM error	Std-CGM error	GCD-CGM error	GCD/FDM gain
6	3.35×10^{-1}	1.531×10^{-1}	4.91×10^{-3}	68.2×
8	2.56×10^{-1}	9.243×10^{-2}	4.66×10^{-3}	54.9×
11	1.93×10^{-1}	5.395×10^{-2}	4.60×10^{-3}	41.9×
16	1.39×10^{-1}	2.930×10^{-2}	4.60×10^{-3}	30.3×

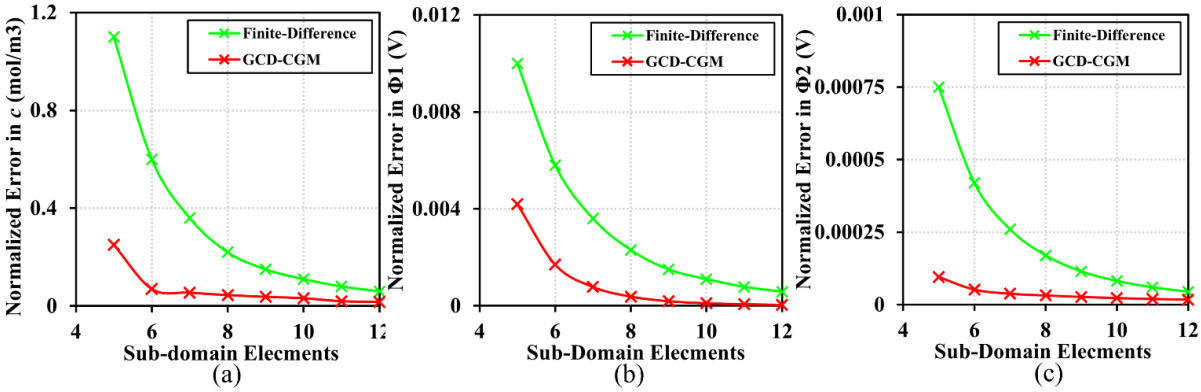


Figure 7 - Normalized state-variable errors obtained using finite-difference and GCD-CGM discretization: (a) electrolyte concentration c, (b) solid-phase potential ϕ_1, and (c) electrolyte-phase potential ϕ_2.

The normalized state errors in Fig. 7 show that GCD-CGM converges faster than FDM for all internal variables. The improvement is particularly evident for the electrolyte concentration and solid-phase potential, where the proposed method reaches a lower error level with fewer sub-domain elements. This confirms that the proposed solver does not only improve terminal voltage accuracy but also preserves the internal electrochemical state behavior required for advanced estimation and control applications.

Overall Numerical Assessment

Table 8 compares the numerical schemes in terms of their representations, observed errors, and available computational evidence. No timing measurements are used.

The comparative summary in Table 8 consolidates the main numerical findings. The L1 scheme is reliable but computationally expensive due to history-dependent convolution. The standard CGM is efficient for smooth integer-order solutions but loses spectral accuracy when the response contains fractional powers. The proposed GCD-CGM resolves this limitation by using the fractional basis

$$\Phi_j(t) = T_j\left[2\left(\frac{t}{T_f}\right)^{\beta} - 1\right], \qquad \beta = \frac{1}{q} \tag{49}$$

which spans $\left\{t^{k\beta}\right\}$. The Caputo derivative can be evaluated termwise, although negative powers may arise outside the finite trial space. This formulation achieves a smaller reported error at matched degrees of freedom, while runtime and conditioning advantages require separate numerical tests.

CONCLUSIONS

The principal findings of the comparison between the finite-difference L1 method, the standard Chebyshev–Galerkin method (CGM), and the proposed generalized Chebyshev denominator-based method (GCD-CGM) are summarized as follows. Percentages refer to the specific numerical settings reported in the tables, rather than to measured execution-time savings.

- At a fractional order of $\alpha = 0.75$ and a matched resolution of seven degrees of freedom, GCD-CGM attains a maximum voltage error of 4.242×10^{-3}, compared with

Table 8 – Qualitative comparison of the three reported solvers; CPU runtimes were not measured.

Method	Representation	Observed error behavior	Cost assessment
FDM L1	Time-grid history convolution	Algebraic convergence trend in Fig. 4	Many DOFs in the reported accuracy comparison; actual CPU time unreported
Standard CGM	Integer-power Chebyshev basis	Slower error decay for the tested fractional response	Fewer DOFs than FDM; actual CPU time unreported
GCD-CGM	Matched fractional-power Chebyshev basis	Rapid low-order error decrease followed by the plateau in Table 6	Smallest reported errors at matched DOFs; actual CPU time unreported

1.16559×10^{-1} for standard CGM. This is a 96.4% reduction in the reported maximum error at equal degrees of freedom (Table 6).

- For the voltage-response comparison, GCD-CGM with nine degrees of freedom has an error of 4.61×10^{-3}, whereas the L1 solution with 501 degrees of freedom has an error of 8.87×10^{-3}. In these particular tests, the GCD approximation uses 98.2% fewer degrees of freedom and shows an approximately 48.0% lower error; these figures do not establish an equivalent CPU-time reduction (Fig. 2).

- For $\alpha = 0.75$, the predicted terminal voltage is 2.359943 V for GCD-CGM and 2.359918 V for the reported L1 calculation at $T = 1$ s. The corresponding charging fractions are 47.1989% and 47.1984% of the 5 V source voltage, respectively (Table 5).

- The GCD-CGM error reaches its lowest tabulated value of 4.242×10^{-3} at $N = 6$ and subsequently levels off near 4.6×10^{-3} for higher tested orders. The evidence therefore supports rapid initial error reduction, but not a demonstrated asymptotic spectral-convergence rate (Table 6).

- The fractional-power trial basis and graded quadrature provide a compact representation of the tested charging response. Nevertheless, the plateau's cause, numerical conditioning, and processor runtime have not been established. In addition, the $\alpha = 0.65$ case requires recalculation with the prescribed $\beta = 0.05$ before it can be used as evidence for the exact matched-basis construction (Table 5).

Future Work

The first priority is a reproducible numerical verification of the corrected square Galerkin system and L1 discretization, including a new calculation for $\alpha = 13/20$ with $\beta = 1/20$. Independent refinement of the quadrature order, reference time step, and arithmetic precision will then be used to investigate the observed error floor and quantify convergence and conditioning.

A second priority is a fair computational-cost study of the L1, standard CGM, and GCD-CGM implementations on identical hardware, with matched accuracy targets and separate measurements of assembly time, solution time, and memory usage. Subject to this validation, the framework may be extended to nonlinear, state-dependent supercapacitor parameters, coupled cell models, and rational approximations to non-rational fractional orders. Finally, experimental or hardware-in-the-loop tests using representative eVTOL power-demand transients should assess prediction accuracy and the feasibility of embedded real-time implementation.

Author Contributions: Conceptualization, A.T.M., O.M. and A.H.H.; formal analysis, A.T.M., A.M.T. and A.E.; methodology, A.T.M., A.M.T., K.K. and A.H.H.; software, A.T.M.,

A.E. and K.K.; supervision, O.M. and A.H.H.; validation, A.T.M., A.E. and O.M.; visualization, A.M.T. and A.E.; writing – original draft, A.T.M., A.M.T. and A.E.; writing – review and editing, O.M., A.H.H., A.T.M. and K.K.

References

[1] He, J., Q. He, Z. Xu, Y. Jia, J. Wang, K. Li, and W. Tan. "Key technologies and upgrade strategies for eVTOL aircraft energy storage systems." *Journal of Energy Storage* 103 (2024): 114402. https://doi.org/10.1016/j.est.2024.114402

[2] Gopi, C. V. V. M. and R. Ramesh. "Review of battery-supercapacitor hybrid energy storage systems for electric vehicles." *Results in Engineering* 24 (2024): 103598. https://doi.org/10.1016/j.rineng.2024.103598

[3] Guo, L., P. Hu, and H. Wei. "Development of supercapacitor hybrid electric vehicle." *Journal of Energy Storage* 65 (2023): 107269. https://doi.org/10.1016/j.est.2023.107269

[4] Zhang, L., X. Hu, Z. Wang, F. Sun, and D. G. Dorrell. "Fractional-order modeling and state-of-charge estimation for ultracapacitors." *Journal of Power Sources* 314 (2016): 28–34. https://doi.org/10.1016/j.jpowsour.2016.01.066

[5] Wu, B., M. Parkes, V. Yufit, L. O. Benedetti, S. Veismann, C. Wirsching, F. Vesper, R. Martinez-Botas, A. Marquis, G. Offer, and N. Brandon. "Design and testing of a 9.5 kwe proton exchange membrane fuel cell–supercapacitor passive hybrid system." *International Journal of Hydrogen Energy* 39, no. 15 (2014): 7885–7896. https://doi.org/10.1016/j.ijhydene.2014.03.083

[6] Zubieta, L. and R. Bonert. "Characterization of double-layer capacitors for power electronics applications." *IEEE Transactions on Industry Applications* 36, no. 1 (2000): 199–205. https://doi.org/10.1109/28.821816

[7] Rafik, F., H. Gualous, R. Gallay, A. Crausaz, and A. Berthon. "Frequency, thermal and voltage supercapacitor characterization and modeling." *Journal of Power Sources* 165, no. 2 (2007): 928–934. https://doi.org/10.1016/j.jpowsour.2006.12.021

[8] Drummond, R., D. A. Howey, and S. R. Duncan. "Low-order mathematical modeling of electric double layer supercapacitors using spectral methods." *Journal of Power Sources* 277 (2015): 317–328. https://doi.org/10.1016/j.jpowsour.2014.11.116

[9] Verbrugge, M. and H. Gu, "Finite difference routines for one and two dimensional problems utilizing a functional programming style." in *Proc. Douglas N. Bennion Memorial Symp.: Topics Electrochem. Eng.*, 94, 1994, 153–188.

[10] Madabattula, G. and S. K. Gupta, "Modeling of supercapacitor." in *Proc. COMSOL Conf.*, Bangalore, India, 2012.

[11] Allu, S., B. V. Asokan, W. A. Shelton, B. Philip, and S. Pannala. "A generalized multi-dimensional mathematical model for charging and discharging processes in a supercapacitor." *Journal of Power Sources* 256 (2014): 369–382. https://doi.org/10.1016/j.jpowsour.2014.01.054

[12] Romero-Becerril, A. and L. Alvarez-Icaza, "Reduced order dynamical model for supercapacitors." in *Proc. IEEE Int. Conf. Electr. Eng. Comput. Sci. Autom. Control (CCE)*, 2010, 71–76. https://doi.org/10.1109/ICEEE.2010.5608575

[13] Srinivasan, V. and J. Weidner. "Mathematical modeling of electrochemical capacitors." *Journal of the Electrochemical Society* 146, no. 5 (1999): 1650–1658. https://doi.org/10.1149/1.1391821

[14] Johansson, P. and B. Andersson, "Comparison of simulation programs for supercapacitor modeling." Master's thesis, Chalmers Univ. Technol., Sweden, year not stated in the source manuscript.

[15] Nadeau, A., G. Sharma, and T. Soyata, "State-of-charge estimation for supercapacitors: A kalman filtering formulation." in *Proc. IEEE ICASSP*, 2014. https://doi.org/10.1109/ICASSP.2014.6853988

[16] Chaturvedi, N., R. Klein, J. Christensen, J. Ahmed, and A. Kojic. "Algorithms for advanced battery-management systems." *IEEE Control Systems Magazine* 30, no. 3 (2010): 49–68. https://doi.org/10.1109/MCS.2010.936293

[17] Suthar, B., V. Ramadesigan, P. Northrop, B. Gopaluni, S. Santhanagopalan, R. Braatz, and V. Subramanian, "Optimal control and state estimation of lithium-ion batteries using reformulated models." in *Proc. IEEE ACC*, 2013, 5350–5355. https://doi.org/10.1109/ACC.2013.6580673

[18] Fauser, D., J. Beddrich, B. Wohlmuth, and H. Steeb. "A fractional moisture-dependent viscoelasticity model for thermoplastic polymers." *Journal of Rheology* 70, no. 4 (2026): 683–698. https://doi.org/10.1122/8.0001048

[19] Catania, G. and S. Amadori. "Experimental identification of the fractional viscoelastic model of isotropic materials." *International Journal of Engineering Science* 225 (2026): 104547. https://doi.org/10.1016/j.ijengsci.2026.104547

[20] Heaviside, O. *Electromagnetic Theory*. Cosimo Inc., 2008, 3.

[21] Tarasov, V. E. "On history of mathematical economics: Application of fractional calculus." *Mathematics* 7, no. 6 (2019): 509. https://doi.org/10.3390/math7060509

[22] Chow, T. "Fractional dynamics of interfaces between soft nanoparticles and rough substrates." *Physics Letters A* 342 (2005): 148–155. https://doi.org/10.1016/j.physleta.2005.05.045

[23] Muthu, S. "New delay-dependent uniform stability criteria for fractional-order bam neural networks with discrete and distributed delays." *Network: Computation in Neural Systems* 37, no. 2 (2026): 419–443. https://doi.org/10.1080/0954898X.2024.2448534

[24] Ruzhansky, M., D. Serikbaev, and N. Tokmagambetov. "An inverse problem for the pseudo-parabolic equation for laplace operator." *International Journal of Mathematics and Physics* 10, no. 1 (2019): 23–28. https://doi.org/10.26577/ijmph-2019-i1-3

[25] Elma, B. and E. Misirli. "On the physical behaviours of the conformable fractional modified camassa–holm equation using two efficient methods." *International Journal of Mathematics and Physics* 12, no. 1 (2021): 19–24. https://doi.org/10.26577/ijmph.2021.v12.i1.03

[26] Khader, M. "Numerical treatment for solving fractional riccati differential equation." *Journal of the Egyptian Mathematical Society* 21, no. 1 (2013): 32–37. https://doi.org/10.1016/j.joems.2012.09.005

[27] Kazem, S., S. Abbasbandy, and S. Kumar. "Fractional-order legendre functions for solving fractional-order differential equations." *Applied Mathematical Modelling* 37, no. 7 (2013): 5498–5510. https://doi.org/10.1016/j.apm.2012.10.026

[28] Doha, E., A. Bhrawy, and S. Ezz-Eldien. "Efficient chebyshev spectral methods for solving multi-term fractional order differential equations." *Applied Mathematical Modelling* 35, no. 12 (2011): 5662–5672. https://doi.org/10.1016/j.apm.2011.05.011

[29] Bhrawy, A. and A. Alofi. "The operational matrix of fractional integration for shifted chebyshev polynomials." *Applied Mathematics Letters* 26, no. 1 (2013): 25–31. https://doi.org/10.1016/j.aml.2012.01.027

[30] Akrami, M. H., M. H. Atabakzadeh, and G. H. Erjaee. "The operational matrix of fractional integration for shifted legendre polynomials." *Iranian Journal of Science and Technology, Transactions A: Science* 37, no. 4 (2013): 439–444.

[31] Tankeyeva, A. K. and S. T. Mynbayeva. "A computational method for solving a boundary value problem for impulsive integro-differential equation." *International Journal of Mathematics and Physics* 14, no. 1 (2023): 45–52. https://doi.org/10.26577/ijmph.2023.v14.i1.03

[32] Momani, S. and R. Qaralleh. "An efficient method for solving systems of fractional integro-differential equations." *Computers & Mathematics with Applications* 52, no. 3–4 (2006): 459–470. https://doi.org/10.1016/j.camwa.2006.02.011

[33] Javeed, S., D. Baleanu, A. Waheed, M. S. Khan, and H. Affan. "Analysis of homotopy perturbation method for solving fractional order differential equations." *Mathematics* 7, no. 1 (2019): 40. https://doi.org/10.3390/math7010040

[34] Diethelm, K. and N. J. Ford. "Analysis of fractional differential equations." *Journal of Mathematical Analysis and Applications* 265, no. 2 (2002): 229–248. https://doi.org/10.1006/jmaa.2000.7194

[35] Nazari, D. and S. Shahmorad. "Application of the fractional differential transform method for fractional-order integro-differential equations with nonlocal boundary conditions." *Journal of Computational and Applied Mathematics* 234, no. 3 (2010): 883–891. https://doi.org/10.1016/j.cam.2010.01.053

[36] Youssri, H. Y. and A. G. Atta. "Chebyshev petrov–galerkin method for nonlinear time-fractional integro-differential equations with a mildly singular kernel." *Journal of Applied Mathematics and Computing* 71, no. 3 (2025): 3891–3911. https://doi.org/10.1007/s12190-025-02371-w

[37] Kilic, M., M. Z. Bazant, and A. Ajdari. "Steric effects in the dynamics of electrolytes at large applied voltages. ii. modified poisson–nernst–planck equations." *Physical Review E* 75, no. 2 (2007): 021503. https://doi.org/10.1103/PhysRevE.75.021503

[38] Lin, Y. and C. Xu. "Finite difference/spectral approximations for the time-fractional diffusion equation." *Journal of Computational Physics* 225, no. 2 (2007): 1533–1552. https://www.sciencedirect.com/science/article/pii/S0021999107000678

[39] Koroche, K. A. "Lax–wendroff difference scheme with richardson extrapolation method for one-dimensional wave equation subjected to integral condition." *International Journal of Mathematics and Physics* 12, no. 2 (2021): 8–22. https://doi.org/10.26577/ijmph.2021.v12.i2.02

Information about authors

Ahmed Taleb Mohamed *– Assistant Lecturer, Faculty of Engineering, Cairo University, Giza, Egypt; e-mail:* ahmedtaleb@cu.edu.eg.

Omar Mokhtar *– Assistant Professor, Department of Physics and Engineering Mathematics, Faculty of Engineering–Mataria, Capital University (formerly Helwan University), Cairo 11718, Egypt; e-mail:* omarmokhtar@m-eng.helwan.edu.eg.

Ahmed M. Taiea *– Assistant Lecturer, Mechanical Power Engineering Department, Faculty of Engineering–Mataria, Capital University (formerly Helwan University), Cairo 11718, Egypt; PhD student, Department of Mechanical and Energy Engineering, Southern University of Science and Technology, Shenzhen 518055, China; e-mail:* ahmedm.abdo@m-eng.capu.edu.eg.

Ayoub Elajjani *– Postdoctoral Fellow, Department of Mechanical and Energy Engineering, Southern University of Science and Technology, Shenzhen 518055, China; e-mail:* ayoub@xs.ustb.edu.cn.

Kairzhan Karzhaubayev *– Assistant Professor, Farabi University, Almaty, Kazakhstan; Assistant Professor, International Engineering and Technological University, Almaty, Kazakhstan; e-mail:* karzhaubayev.k@kaznu.kz, kk.karzhaubayev@metu.edu.

Alamir H. Hassan *– Assistant Professor, Mechanical Power Engineering Department, Faculty of Engineering–Mataria, Capital University (formerly Helwan University), Cairo 11718, Egypt; Postdoctoral Fellow, Department of Mechanical and Energy Engineering, Southern University of Science and Technology, Shenzhen 518055, China; e-mail:* alamirhoussin@m-eng.capu.edu.eg.